*Graphical Abstract (for review)

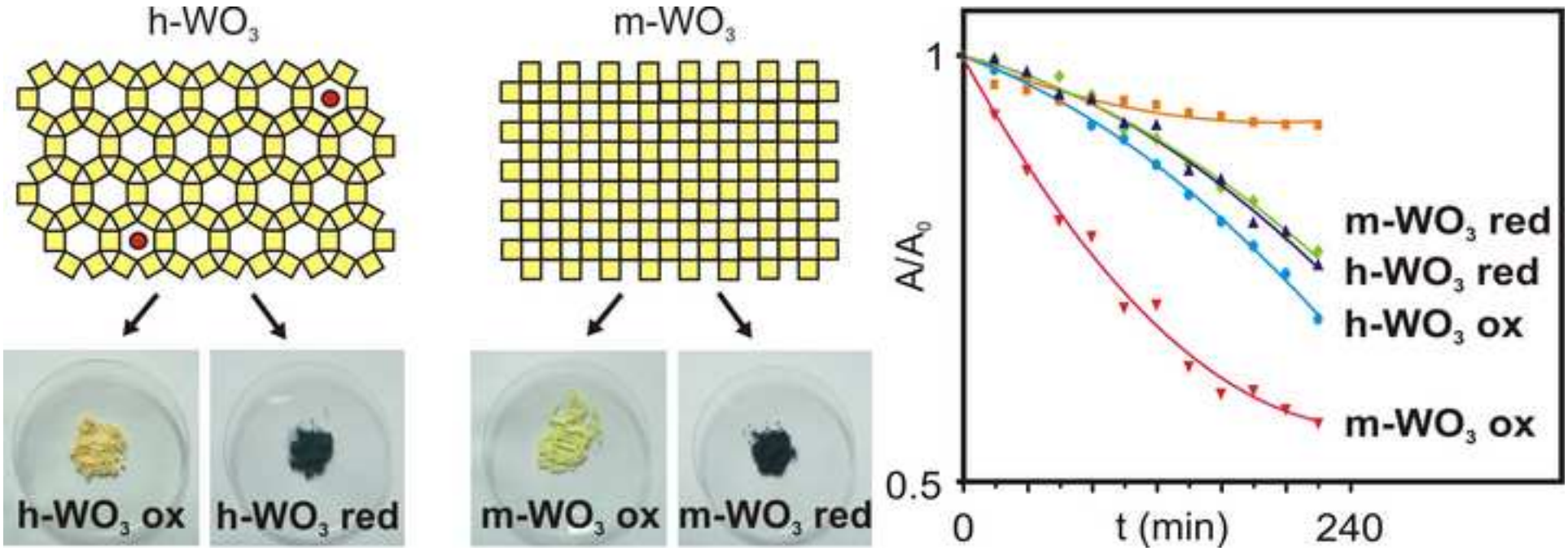

Graphical abstract

Oxidized/partially reduced hexagonal (h-) and monoclinic (m-) WO_3 nanoparticles were tested as photocatalysts both in the aqueous and gas phase. Unlike other semiconductor oxides, WO_3 is unique in that its composition is decisive on photocatalysis, while its crystal structure has only an indirect role.

Highlights

- Oxidized/partially reduced h- and m-WO_3 nanoparticles were prepared.
- Composition is decisive for WO_3: the more oxidized, the better photocatalyst.
- Crystal structure of WO_3 has only secondary role through affecting composition.
- Lower activity of reduced WO_3 is due to W^{5+}/W^{4+} atoms and less surface OH.
- We predict that tungsten bronzes and cubic WO_3 are worse photocatalysts than m-WO_3.

WO_3 photocatalysts: influence of structure and composition

Imre M. Szilágyi[1,2,3*], Balázs Fórizs[1], Olivier Rosseler[4], Ágnes Szegedi[5], Péter Németh[5], Péter Király[6], Gábor Tárkányi[6], Balázs Vajna[7], Katalin Varga–Josepovits[8], Krisztina László[9], Attila L. Tóth[10], Péter Baranyai[11], Markku Leskelä[3]

[1]Department of Inorganic and Analytical Chemistry, Budapest University of Technology and Economics, H–1111 Budapest, Szt. Gellért tér 4. Hungary; [2]Research Group of Technical Analytical Chemistry of the Hungarian Academy of Sciences, Budapest University of Technology and Economics, H–1111 Budapest, Szt. Gellért tér 4., Hungary; [3]Department of Chemistry, University of Helsinki, Helsinki, P.O. Box 55, FI-00014, Finland; [4]LMSPC, UMR 7515 du CNRS, ECPM, ULP, 25, rue Becquerel, 67087 Strasbourg Cedex 2, France; [5]Institute of Materials and Environmental Chemistry, Research Centre of Natural Sciences, Hungarian Academy of Sciences, H–1025 Budapest, Pusztaszeri út 59–67. Hungary; [6]Institute of Organic Chemistry, Research Centre of Natural Sciences, Hungarian Academy of Sciences, H–1025 Budapest, Pusztaszeri út 59–67. Hungary; [7]Department of Organic Chemistry and Technology, Budapest University of Technology and Economics, H–1111 Budapest, Budafoki út 8. Hungary; [8]Department of Atomic Physics, Budapest University of Technology and Economics, H–1111 Budapest, Budafoki út 8. Hungary; [9]Department of Physical Chemistry and Materials Science, Budapest University of Technology and Economics, P.O. Box 92, H–1521 Budapest, Hungary; [10]Institute for Technical Physics and Materials Science, Research Centre of Natural Sciences, Hungarian Academy of Sciences, H–1121 Konkoly–Thege út 29–33. Budapest, Hungary; [11]Institute of Molecular Pharmacology, Research Centre of Natural Sciences, Hungarian Academy of Sciences, H–1025 Budapest, Pusztaszeri út 59–67. Hungary

* Tel: +36-1-463-4047; Fax: +36-1-463-3408; E-mail address: imre.szilagyi@mail.bme.hu (I.M. Szilágyi)

Abstract

Hexagonal (h–) and monoclinic (m–) WO_3 nanoparticles were prepared with controlled composition (oxidized/yellow color or partially reduced/blue color) through annealing $(NH_4)_xWO_{3-y}$. The formation, structure, composition, morphology and optical properties of the samples were analyzed

by powder XRD, SEM, TEM–ED, Raman, XPS, ^{1}H–MAS NMR, diffuse reflectance UV–VIS and photoluminescence (PL) spectroscopy. Their photocatalytic properties were tested by decomposing methyl–orange in the aqueous phase, and acetone in the gas phase. Oxidized m–WO_3 (**m-WO_3 ox**) was the most active photocatalyst both in the aqueous and gas phase, followed by the oxidized h–WO_3 (**h-WO_3 ox**) sample. Reduced h–WO_3 (**h-WO_3 red**) and m–WO_3 (**m-WO_3 red**) exhibited much lower activities. Thus, in contrast to TiO_2, where crystalline structure (rutile or anatase) plays a key effect in photocatalysis, for WO_3 it is the composition which is of greatest importance: the more oxidized the WO_3 sample, the better photocatalyst it is. The crystal structure of WO_3 has only an indirect effect in that it influences the composition of WO_3 samples. While oxidized m–WO_3 is completely oxidized, oxidized h–WO_3 is always in a partially reduced state due to the presence of stabilizing positive ions in its hexagonal channels. Consequently, an oxidized monoclinic WO_3 material will always perform better photocatalytic activity than an oxidized hexagonal one.

Keywords: Photocatalysis; WO_3; Hexagonal; Monoclinic

1. Introduction

The use of metal oxide semiconductors (MOS) as photocatalysts offer an environmental friendly way to clean surfaces or water by decomposing the organic contaminations with solar energy [1]. The most studied photocatalyst is TiO_2 as its valence and conductance energy levels are suitable for both oxidation and reduction of water molecules (water splitting) [2–10]. Besides TiO_2, the photocatalytic activities of several other MOS have also been studied (pl. V_2O_5, WO_3, ZnO, ZrO_2) [11–15]. The only drawback of TiO_2 is that it absorbs only in the UV range. However, WO_3 can absorb also visible light to some extent, making it the second most studied MOS photocatalyst. Several factors have been reported to influence the photocatalytic activity of various MOS, e.g. the intensity and spectrum of the irradiating lamp [16–18]; pH [19,20]; temperature [8]; concentration [18]; composition [8–10], particle size [21] and crystal structure [8,22–24] of the catalyst; presence of oxidizing agents [8,19] or inorganic ions [19,25,26]. In the case of TiO_2 it is well known that its different crystalline polymorphs have different photocatalytic activity, i.e. anatase is a better photocatalyst than rutile [27].

WO_3 has also several crystalline modifications (triclinic, monoclinic, orthorombic, tetragonal, hexagonal, cubic). The triclinic, monoclinic, orthorombic and tetragonal WO_3 phases have basically the same chessboard–like arrangement of WO_6 octahedra, thus they can transform reversibly into each

other. They differ only in the extent to which the W atoms are displaced from the center of WO_6 octahedra [28,29]. Hence, WO_3 has only three truly different crystalline arrangements (the monoclinic/triclinic/orthorhombic/tetragonal, the hexagonal and the cubic). Up to now only WO_3 samples belonging to the triclinic/monoclinic/orthorhombic/tetragonal phases have been reported as a photocatalysts [18,30–33].

Thus, it was not clear what the photocatalytic properties of the second most studied phase of WO_3, i.e. hexagonal WO_3, were. In addition, the influence of the composition of WO_3 (completely oxidized or partially reduced) on its photocatalytic activity has not been studied either. Recent studies revealed that in gas sensing both the crystal structure (monoclinic or hexagonal) and also the composition (oxidized or partially reduced) of WO_3 made large differences [34,35], and similar effects could be expected in photocatalysis. Therefore, the present study aims to find answers to the influence of structure and composition of WO_3 on its photocatalytic properties.

Hence, monoclinic and hexagonal WO_3 with two different compositions (oxidized/yellow color and reduced/blue color) were prepared through annealing hexagonal ammonium tungsten bronze, $(NH_4)_xWO_{3-y}$. We have selected this preparation route among the several different reported ones (e.g. microwave hydtrothermal treatment [36], acidic hydrothermal precipitation reaction [37], thermal annealing [35]), as this method provided control on the composition and morphology of h–WO_3 [35]. We intended to extend this route for controlling the composition and morphology of m–WO_3 as well. We optimized the annealing conditions of $(NH_4)_xWO_{3-y}$ through thermal studies (TG/DTA) in order to obtain the WO_3 samples with appropriate crystal structures and compositions. Consecutively, powder X–ray diffraction (XRD), scanning (SEM) and transmission electron microscopy (TEM) combined with electron diffraction (ED), as well as Raman, X–ray photoelectron (XPS), diffuse reflectance UV–VIS and photoluminescence (PL) spectroscopy were used to investigate the structure, morphology, composition and optical properties of the as–prepared WO_3 samples. To study how the composition and crystal structure of WO_3 influence its photocatalytic property, we studied the WO_3 samples as photocatalysts by decomposing methyl–orange in the aqueous phase and acetone in the gas phase.

2. Experimental

2.1. Sample preparation

Hexagonal (h–) WO_3 (**h-WO_3 ox** and **h-WO_3 red**) and monoclinic (m–) WO_3 (**m-WO_3 ox** and **m-WO_3 red**) samples with oxidized (yellow color) or partially reduced (blue color) W oxidation states (Fig. 1a-b) were prepared by annealing hexagonal ammonium tungsten bronze, $(NH_4)_xWO_{3-y}$ in air and N_2. ($(NH_4)_xWO_{3-y}$ was prepared by the partial reduction of ammonium paratungstate tetrahydrate, $(NH_4)_{10}[H_2W_{12}O_{42}]\cdot 4H_2O$ (APT), in H_2 for 6 h at 400 °C [38]). Table 1 contains the preparation conditions (decomposition atmosphere and temperature) for the h–WO_3 and m–WO_3 samples. These conditions were determined by measuring the thermal decomposition of the precursor $(NH_4)_xWO_{3-y}$ by TG/DTA in air and N_2 (Fig. S1 in Supporting information).

2.2. Characterization

The thermoanalytical (TG/DTG/DTA) curves of the precursor $(NH_4)_xWO_{3-y}$ were recorded with an STD 2960 Simultaneous DTA/TGA (TA Instruments Inc.) thermal analyzer. During the measurements in an open platinum crucible, sample sizes of ca. 150 mg, a heating rate of 10 °C min^{-1}, flowing air or N_2 (130 ml min^{-1}) purges were used.

Powder X–ray diffraction (XRD) patterns were measured by a PANalytical X'pert Pro MPD X–ray diffractometer using Cu Kα radiation.

Raman spectra were collected by a Jobin Yvon Labram instrument attached to an Olympus BX–41 microscope. The samples were examined with a frequency doubled Nd–YAG laser (532 nm). Measurement time varied between 0.6 s and 150 s according to the applied laser power and the Raman activity of the samples.

N_2–BET specific surface measurements were conducted on a Quantachrome NOVA 2000E device. In the specific surface area (S_{BET}) calculation, a multipoint regression was used, as the value of the BET constant (C) was too small.

Scanning electron microscopy (SEM) characterization was performed by a LEO–1550 FEG SEM instrument.

Transmission electron microscopy (TEM) images and electron diffraction (ED) patterns were recorded on a FEI Morgagni 268D instrument.

X–ray Photoelectron (XPS) spectra were recorded by a VG Microtech instrument consisting of a XR3E2 X–ray source, a twin anode (Mg K_α and Al K_α) and a CLAM 2 hemispherical analyzer using Mg K_α radiation. Detailed scans were recorded with 50 eV pass energy at (0.05 eV/1.5 s). The spectrometer was calibrated with the binding energy of the C1s line (285 eV).

Solid state ^{1}H–MAS (magic angle spinning) NMR experiments were carried out on a VARIAN NMR SYSTEM spectrometer (600 MHz for 1H) using a 3.2 mm HXY VARIAN/Chemagnetics probe. ^{1}H chemical shifts were referenced to adamantane (δ^{1}H = 0 ppm). Background suppression DEPTH [39] was employed to remove signals from the probe.

Diffuse reflectance UV–VIS absorption spectra of solid samples were recorded on a Cary 100 UV–VIS spectrometer (Varian), equipped with a DRA–CA–30I integrating sphere for solid phase characterization.

Photoluminescence (PL) spectra were measured on a Perkin Elmer LS 50 B instrument at excitation wavelengths of 230, 270 and 340 nm.

2.3. Photocatalysis

The fluid phase photocatalytic tests were performed in a cylindrical, termostated (25 °C), inner lamp type, 350 ml Heraeus UV–Reactor System 1 reactor (Fig. S2 in Supporting information) using magnetic stirring and oxygen bubbling (100 ml/min). The reaction mixture was irradiated with a Heraeus TQ 150 Z2 Hg lamp, which had its main emission ranges between 250–360 nm and 500–550 nm. In the photocatalytic tests, methyl orange (10 mg/350 ml H_2O) was decomposed. In the pre–tests, a higher WO_3 powder concentration (350 mg/350 ml, i.e. the usual 1 g/l) was also tried, but in this case a part of the powder precipitated, therefore we applied lower powder concentration (100 mg/350 ml). During the tests the pH remained constant. At first, the reaction mixture was stirred in the dark for 10 minutes in order to reach adsorption equilibrium. Then, after switching on the lamp and waiting 4 minutes for its warming up, 2–3 ml intermediate samples were taken from the reaction mixture every 20 minutes with a syringe equipped with a membrane filter (Sigma Aldrich, Iso–Disc, PTFE, 0.45 μm pore size) during the 220 minute long tests.

The intermediate samples were analyzed by a Jasco V–550 UV–VIS spectrophotometer between 200–700 nm, and the degradation of methyl orange was determined at the wavelength of its maximum absorption (465 nm). The absorbance of methyl orange depended linearly on its concentration according to Lambert–Beer's law, thus it was an appropriate method to monitor the decomposition of the dye.

The gas phase photocatalytic reactor used in this study was made of 2 concentric tubes (Fig. S3 in Supporting information). The reactant gaseous mixture was flowed between the internal quartz tube (22 mm diameter) and the external Pyrex tube (29 mm diameter). The light sources were inserted inside the internal quartz tube. The UV lamp was a commercial black light (8 W, Philips) with a spectral peak

centered around 365 nm, and the VIS lamp (8W, Sylvania) had emission spectrum between 380–700 nm. The inner side of the external Pyrex tube was evenly coated by a slurry containing WO_3 powder (300 mg in 20 mL of ethanol), then the solvent was evaporated to dryness at 25 °C, and the coated reactor was further dried at 110 °C for 1 h in air. The acetone containing gas flow was generated by bubbling air through acetone in a saturator. Relative humidity (RH) was adjusted by flowing air through a water containing saturator. The total gas flow rate was adjusted at 200 mL/min. The concentration of acetone was 1800 ppm (4.35 mg/L) and relative humidity was changed between 0–50%. The photocatalytic reaction products were analyzed by a microgaschromatograph (MTI Quad400P) equipped with a thermal conductivity detector suitable for organics, H_2O and CO_2 quantification.

3. Results and discussion

3.1. Structure

The structure of the WO_3 samples was analyzed by XRD and Raman spectroscopy. Powder XRD patterns (Fig. 1c) revealed that **h-WO_3 ox** and **h-WO_3 red** consisted of pure h–WO_3 (ICDD 85–2460), while **m-WO_3 ox** and **m-WO_3 red** were made of pure m–WO_3 (ICDD 43–1035). The XRD peaks of oxidized samples (**h-WO_3 ox**, **m-WO_3 ox**) were sharper and had greater intensities than the reduced samples (**h-WO_3 red**, **m-WO_3 red**). This showed that the lattice of the reduced samples was distorted, as they had an oxygen deficient structure. In addition, **m-WO_3 red** showed a preferred orientation along the (020) axis.

Raman spectra (Fig. 1d) confirmed our XRD results. Generally, compared to XRD, Raman spectroscopy is more sensitive to the presence of m–WO_3 in h–WO_3 (m–WO_3 is the decomposition product of h–WO_3) [35,40]. But even according to Raman spectra, **h-WO_3 ox** and **h-WO_3 red** were found to be pure h–WO_3, while **m-WO_3 ox** and **m-WO_3 red** were made of pure m–WO_3. In the Raman spectrum of the oxidized hexagonal WO_3 sample (**h-WO_3 ox**) the main bands at 786, 693, 651 cm^{-1} were characteristic to the O–W–O stretching vibrations [35,41–43]. The bands at 327 and 263 cm^{-1} were identified as O–W–O deformation vibrations. The peak at 185 cm^{-1} was a lattice vibration of the hexagonal WO_3 structure. The most intensive bands of the oxidized monoclinic WO_3 sample (**m-WO_3 ox**) at 806 and 714 cm^{-1} were O–W–O stretching vibrations [35,41–44]. The different positions and numbers (three by h–WO_3 and two by m–WO_3) of these stretching vibrations between 810–650 cm^{-1} are the easiest way to differentiate h–WO_3 from m–WO_3 based on Raman spectra. The positions of the O–

W–O deformation vibrations (329 and 268 cm^{-1}) by **m-WO_3 ox** were similar as in the case of **h-WO_3 ox**.

The distorted structure of the reduced WO_3 samples (**h-WO_3 red**, **m-WO_3 red**) was also reflected by their Raman spectra. Their Raman peaks were considerably more diffuse than in the case of the oxidized WO_3 samples (**h-WO_3 ox**, **m-WO_3 ox**), and some peaks were not even visible as they overlapped with others (e.g. by **h-WO_3 red** the two deformation vibrations around 690 and 650 cm^{-1} overlapped and only one peak at 694 cm^{-1} was observable). As large amounts of reduced tungsten atoms (W^{4+}, W^{5+}) were also present in the reduced WO_3 samples, the measurement times significantly increased. E.g. 0.6 s was needed for **m-WO_3 ox**, while 150 s was the total measurement time for **m-WO_3 red**. This is due to the fact that the different oxygen deficiencies of the samples changed the polarizability and thus the Raman intensity of the related bonds [45]. The shift of the most intensive Raman bands also evidenced the different oxidation states of the samples. The chemical bonds of W^{6+} were stronger than those of reduced tungsten atoms (i.e. W^{5+} and W^{4+}), thus Raman peaks of W^{6+} bonds appeared at higher energies, i.e. higher wavenumbers [43]. As a result, for the hexagonal WO_3 samples the main peak shifted from 776 cm^{-1} by **h-WO_3 red** to 786 cm^{-1} by **h-WO_3 ox**, and for the monoclinic WO_3 samples it shifted from 801 cm^{-1} by **m-WO_3 red** to 806 cm^{-1} by **m-WO_3 ox**.

3.2. Morphology

The morphology of the WO_3 samples was studied by low temperature (77 K) N_2–adsorption, SEM and TEM–ED. **m-WO_3 ox** had the lowest specific surface area calulcated from the BET model (S_{BET}), i.e. 6.5 m^2/g, while the surface area of the other samples was between 11–13 m^2/g (Table 1). The mean particle size was estimated from the S_{BET} values assuming spherical particle geometry, and 7.16 g/cm^3 was taken as the density of $\rho(WO_3)$ [46]. Corroborating S_{BET} data, **m-WO_3 ox** had the largest mean particle size (d = 129 nm), while the particle size varied between 64–76 nm for the other samples (Table 1).

SEM images revealed that **m-WO_3 ox** consisted of 60–90 nm particles, while the other samples had 50–70 nm particles, i.e. s SEM also evidenced that the particles of **m-WO_3 ox** were slightly larger than that of the other samples (Fig. 2, Table 1). N_2–BET data showed somewhat larger particles than SEM, but this is due to the fact that the particles were highly aggregated and intergrown, forming micrometer scale blocks, and this reduced the specific surface, and increased their apparent S_{BET} values. According to the SEM results, the particle size remained the same, when **h-WO_3 ox**, **h-WO_3 red** and **m-**

WO_3 red were prepared from $(NH_4)_xWO_{3-y}$, while for **m-WO_3 ox** it increased. It was previously observed that when 50–100 nm hexagonal WO_3 particles were heated in air at 900 °C, 100–500 nm monoclinic WO_3 particles were formed. It was found that crystallization of the more stable m–WO_3 from h–WO_3 and the further annealing of m–WO_3 were responsible for the growth of the particle size [40]. Here in the case of **m-WO_3 ox**, a similar process (recrystallization and oxidation of m–WO_3 from $(NH_4)_xWO_{3-y}$/h–WO_3 and the isotherm heating at 600 °C for 0.5 h) seems to be responsible for the larger particle size.

The particle sizes measured by TEM (Fig. 3, Table 1) were the same as by SEM. ED patterns showed the most intense, characteristic reflections of different WO_3 forms and confirmed the appropriate (hexagonal or monoclinic WO_3) structures. On the HRTEM images, the observed lattice distances matched the (100) reflection of h–WO_3, and the (020) reflection of m–WO_3. ED patterns and HRTEM images also revealed that the samples were well ordered. Even **m-WO_3 red** was found to be crystalline on HRTEM images, though its XRD pattern showed an almost amorphous structure, which could mean that this sample was ordered only on the scale of a few nanometers. As an interesting feature, we could not observe the lattice planes on HRTEM images of **m-WO_3 ox**, which was probably due to its larger particle size.

3.3. Composition

The composition of the WO_3 samples was investigated by XPS and ^{1}H–MAS NMR. The most oxidized sample was **m-WO_3 ox** (Table 1). The as–prepared yellow m–WO_3 samples are theoretically always completely oxidized, containing only W^{6+} atoms, without any W^{5+} or W^{4+} atoms (Table 1). However, in the high vacuum in the XPS device the surface of the otherwise yellow m–WO_3 particles obtained a greenish color. This is explained by that some W atoms on the surface became slightly reduced; in fact we detected 1.8 % W^{5+}. However, this was a measurement error, and **m-WO_3 ox** was completely oxidized, before putting it into the XPS instrument. This is supported by the results of other measurements (e.g. UV-VIS) as well. In the case of the other samples (e.g. **h-WO_3 ox**) we did not notice a color change, i.e. a change in the oxidation state, after the XPS measurement.

h-WO_3 ox was less oxidized (Table 1) and it contained W^{4+} and W^{5+} atoms in addition to W^{6+} [38,47]. In previous studies, it has been shown that h–WO_3 always contains some cation impurities in the hexagonal channels, which are necessary to maintain the hexagonal WO_3 structure (Fig. 1a) [35]. Due to these, the oxidized form of h–WO_3 (**h-WO_3 ox**) is always more reduced than the oxidized form

of m–WO_3 (**m-WO_3 ox**). The reduced samples (**h-WO_3 red, m-WO_3 red**) contained larger amounts of reduced tungsten atoms, which explained their blue color (Table 1, Fig. 1b). **h-WO_3 red** contained some residual stabilizing NH_4^+ ions, and it was not annealed in an oxidizing atmosphere, as **h-WO_3 ox**, which explains why it was more reduced than **h-WO_3 ox**. When **m-WO_3 red** was prepared, all the residual NH_4^+ ions were removed thermally; either by releasing NH_3 and leaving a proton in the structure, or releasing NH_3 and H_2O paralelly. Due to this **m-WO_3 red** became more reduced than **h-WO_3 red**, and thus there were more W^{5+} and W^{4+} atoms in **m-WO_3 red** than in **h-WO_3 red**.

^{1}H–MAS NMR spectra confirmed the presence of NH_4^+ ions (4.1 ppm) and NH_3 molecules (5.2. ppm) in **h-WO_3 ox** and **h-WO_3 red** (Fig. 4). The chemical shifts of NH_4^+ and NH_3 were 0.5.–1.0 ppm lower than previously observed [38,48,49]; nevertheless, a comparison with the ^{1}H–MAS NMR spectrum of the precursor $(NH_4)_xWO_{3-y}$ (Fig. 4), where the positions of NH_4^+ and NH_3 were obvious, made the assignment of these peaks reliable. Based on previous results [38,48,50,51] surface and structural H_2O molecules in tungsten bronzes and oxides can be found anywhere between 4–6 ppm. In our case the peak around 6 ppm was present even by **m-WO_3 ox** and **m-WO_3 red**, in which there was absolutely no space for H_2O in the structure, therefore we assigned this peak to surface H_2O. The origin of the small peak at 1.0 ppm by **h-WO_3 ox** and **h-WO_3 red**, and at –0.3 ppm by $(NH_4)_xWO_{3-y}$ is not yet understood. Previous results [50,51] assigned it to OH surface groups of tungsten oxides, but now it did not appear by **m-WO_3 ox** and **m-WO_3 red**, which are the pure tungsten oxide samples in our study.

3.4. Optical properties

In order to help understand the photocatalytic properties of the WO_3 samples, their UV–VIS absorption and emission spectra were investigated with diffuse reflectance UV–VIS and photoluminescence (PL) spectroscopy. The diffuse reflectance UV–VIS spectra (Fig. 5a) showed that the oxidized samples (**h-WO_3 ox**, **m-WO_3 ox**) absorbed until ca. 500 nm, while the reduced samples (**h-WO_3 red**, **m-WO_3 red**) had absorption in the whole UV–VIS range, though with decreased intensity between 350–500 nm. The dark color (absorption above 500 nm) of the reduced samples is due to the presence of larger amounts of reduced (W^{4+}, W^{5+}) atoms besides W^{6+}, which introduced new discrete energy levels quite deep into the bandgap.

The bandgap energies (2.72 eV and 2.55 eV) were calculated from the absorption edges (λ_{max}) observed at 460 and 490 nm, for **h-WO_3 ox** and **m-WO_3 ox** respectively. The Kubelka Munk functions were determined at 2.76 eV and 2.73 eV, for **h-WO_3 ox** and **m-WO_3 ox** respectively. We note that **h-**

WO_3 ox still contained some reduced tungsten atoms, which were responsible for the small overlapping peak between 400–560 nm. We infer from that secondary absorption the presence of discrete energy levels in the band of **h-WO_3 ox**, 0.59 eV over the valence band (560 nm corresponds to 2.13 eV). The completely oxidized structure of **m-WO_3 ox** was supported by that as well, that it did not have this overlapping peak related to reduced tungsten atoms.

On the one hand, according to the higher absorption of reduced WO_3 samples (**h-WO_3 red**, **m-WO_3 red**) in VIS range, they could be better photocatalysts, than the oxidized samples (**h-WO_3 ox**, **m-WO_3 ox**). On the other hand, the new, quite deep energy levels in their bandgap might act as recombination centers [52–55], which could lower the photocatalytic efficiency. In addition, the increased conductance of the reduced samples (electrons could easily hop between the W atoms of different oxidation states [35]) could result in the easier transport and thus the recombination of electrons and holes.

According to the PL spectra (Fig. 5b), all samples had similar emission peak systems. The blue emission peaks at 409 and 421 nm were assigned to oxygen vacancies or defects [56]. The blue emission peaks at 453 and 487 nm are in the range of the measured bandgap energies and they were explained as band–band transitions [57]. The lower energy green emission peaks at 523 and 535 nm were attributed to localized states in the bandgap [58]. We note that the position and intensity of the emission peaks shifted to some extent if different excitation wavelengths (230 and 270 nm) were used (Fig. S4 in Supporting information).

The reduced samples (**h-WO_3 red**, **m-WO_3 red**) had significantly lower luminescence intensity in the whole spectrum, compared to the oxidized samples (**h-WO_3 ox**, **m-WO_3 ox**). This is due to the fact that the adsorbed light could induce polaron transitions between W^{4+}, W^{5+} and W^{6+} atoms in the reduced samples [59]. Additionally, this means that a smaller portion of the absorbed light could be used to generate holes and electrons, which could take part in photocatalytic processes. Also due to polaron transitions, **h-WO_3 ox**, which was also partially reduced, had lower luminescence intensity, compared to **m-WO_3 ox**. In case of **h-WO_3 red** and **m-WO_3 red**, the peaks belonging to the O vacancies (400–430 nm) were the strongest in their spectrum, which also supported their highly reduced structure. Furthermore, though **h-WO_3 ox** had in general lower luminescence intensity than **m-WO_3 ox**, its peaks belonging to its increased amount of O vacancies were stronger than that of **m-WO_3 ox**.

3.5. Photocatalysis in the gas phase

WO_3 samples were tested as photocatalysts in the gas phase by decomposing acetone in air. The flow–through type reactor was illuminated by either UV or VIS light, and during the tests relative humidity (RH) was varied between 0–50 %. The role of RH was to increase the number of surface OH–groups, which are necessary for photocatalysis [60] (a full monolayer of water is expected to cover the WO_3 surface around 15 % RH [61]). Acetone is miscible with water, therefore it can still diffuse to the surface through the adsorbed H_2O phase to reach the active sites. During the tests, when RH was raised, the amount of produced CO_2 always increased until the CO_2 level reached a plateau showing that the surface of particles was saturated with OH groups. In the summary figure of the gas phase photocatalysis measurements, the curves plot the amount of the decompositon product CO_2 (ppm) versus relative humidity (Fig 6).

In gas phase photocatalytic conversion of acetone, **m-WO_3 ox** turned out to be the most active photocatalyst. Using UV light, it already produced 9 ppm CO_2 at 0 % RH, and the maximum decompositon rate was reached with 20 ppm CO_2 at 8 % RH. With VIS light, the sample was at least as active as with UV, as it produced 8 ppm CO_2 at 0 % RH, and the saturation was at 40 % RH (26 ppm CO_2).

h-WO_3 ox, the other oxidized sample, was the second most active catalyst. With UV, it produced slightly less, i.e 8 ppm CO_2 at 0 % RH. It needed higher RH (20 %) to reach saturation and produce 20 ppm CO_2, compared to **m-WO_3 ox**. With VIS, **h-WO_3 ox** was not active at all in dry atmosphere. It produced CO_2 (6 ppm) only when RH was at least 17 %, and reached saturation at 42 % RH (8 ppm CO_2).

The reduced WO_3 samples (**h-WO_3 red**, **m-WO_3 red**) had much worse catalytic performance than the oxidized ones. With UV light, **h-WO_3 red** and **m-WO_3 red** were not active in dry atmosphere, and they produced only 12 and 11 ppm CO_2, respectively, even at 45 % RH (saturation). Under VIS light they were not active at all, neither in dry, nor in humid atmosphere, though they had considerable absorption in the VIS region.

These results show that acetone seems to interact very weakly with WO_3 directly. On TiO_2, acetone can bind to the surface with Ti^{4+} lattice cations or through H–bonding with Ti–OH groups [60] It seems that in the case or our WO_3 samples, acetone adsorbs preferentially on WO_3 through H–bonding with W–OH groups.

The tests with varying RH levels suggest that **m-WO_3 ox** has the highest amount of surface OH groups, followed by **h-WO_3 ox**. The reduced samples (**h-WO_3 red**, **m-WO_3 red)** have considerably less of them. To check this we measured the amount of surface O^{2-}, OH^- and H_2O species by XPS [62]. The

O1s peak was deconvoluted and the area of the fitted O^{2-}, OH^- and H_2O curves were assumed to be proportional to their amount. In Table 1 the ratio of surface $O^{2-}/OH^-/H_2O$ species is shown, normalized to the amount of O^{2-} in each sample. The results showed that **m-WO_3 ox** had really the highest amount of surface OH groups (and H_2O molecules), followed by **h-WO_3 ox**. The reduced samples had considerably less surface OH species. We assume that if WO_3 is slightly (**h-WO_3 ox**) or significantly reduced (**h-WO_3 red**, **m-WO_3 red**), then the oxygen deficient structures will have less oxygen atoms also on the surface of particles. Hence, the amount of bridging O atoms (W–O–W) and O atoms with double bonds (W=O) will increase on the surface, and the amount of –OH groups will decrease. This is vital information not just for photocatalytic, but for other applications as well (e.g. catalysis, gas sensing).

3.6. Photocatalysis in the aqueous phase

WO_3 samples were tested as photocatalysts in aqueous solution by decomposing methyl orange. Relative absorbance (A/A_0) was used as the ordinate on Fig. 7, so that the photocatalytic properties of the samples could be compared. In the liquid phase the role of relative humidity was eliminated as in water the surface of particles was saturated with OH groups. Methyl orange was selected as a probe molecule, as its absorption maximum (465 nm) was exactly where WO_3 samples had minimum in their UV–VIS spectra.

The degradation effect of the lamp (photolysis) was tested without adding any WO_3 powder. After 220 min reaction time the concentration of methyl orange decreased to 92 % of the original (Fig. 7: MO). Similar to the gas phase, **m-WO_3 ox** had the largest photocatalytic activity, as **m-WO_3 ox** decreased the methyl orange concentration to 57 % after 220 min. Again, **h-WO_3 ox** showed lower activity with 69 % methyl orange concentration at the end of the reaction. The reduced WO_3 samples (**h-WO_3 red**, **m-WO_3 red**) decomposed methyl orange to quite similar degree (75–77 %), and they were both less active, than the oxidized samples.

3.7. Influence of structure and composition of WO_3 on photocatalysis

The results of the gas and aqueous phase photocatalytic tests corroborated each other. In both conditions, the oxidized form of monoclinic WO_3 (**m-WO_3 ox**) was the most active photocatalyst (despite that it had the lowest specific surface area), and the oxidized form of hexagonal WO_3 (**h-WO_3**

ox) was somewhat less active. In contrast, the reduced forms of both monoclinic and hexagonal WO_3 (**h-WO_3 red**, **m-WO_3 red**) had considerably lower photocatalytic activity. From these results we assume that the composition of the WO_3 samples (oxidized or partially reduced) was the decisive factor on their photocatalytic activity. The reason is that there are fewer defects in the lattice of the oxidized samples, compared to the reduced ones, and thus there are less recombination centers, which would be detrimental for photocatalysis. The photocatalytic results are in agreement with our observations on the structure, composition and optical properties of these samples, as they suggested that the oxidized samples would be better photocatalysts, and the oxidized m–WO_3 (**m-WO_3 ox**) might be the best one.

In contrast, the crystal structure of WO_3 had only secondary, indirect role in photocatalysis. It is true that the oxidized m–WO_3 sample (**m-WO_3 ox**) was better photocatalyst than the oxidized h–WO_3 sample (**h-WO_3 ox**). However, this was most probably caused again by the different composition of the samples, and not by their different crystal structure. The explanation is that different compositions belong to hexagonal and monoclinic WO_3. As we found, **m-WO_3 ox** was completely oxidized. In contrast, **h-WO_3 ox** was slightly reduced, i.e. due to the presence of stabilizing impurities (NH_4^+) in the hexagonal channels of h–WO_3, reduced tungsten atoms (W^{4+}, W^{5+}) were also present besides W^{6+} to maintain electroneutrality [35]. Therefore, due to its slightly reduced structure, oxidized hexagonal WO_3 will always be a less active photocatalyst, than the completely oxidized monoclinic WO_3.

To conclude, the different crystalline phases (monoclinic or hexagonal) of WO_3 influenced the photocatalytic activity in very different ways, compared to the different phases of TiO_2 (anatase or rutile). In the case of TiO_2, clearly the different crystal structures of anatase and rutile are responsible for the difference in their photocatalytic activity, as these two phases have exactly the same composition. In contrast, the different structures of the hexagonal and monoclinic WO_3 play only a secondary role in photocatalysis. In reality the composition of a given WO_3 sample is the most important factor influencing photocatalysis: the more oxidized the WO_3 sample, the better photocatalyst it is.

4. Conclusions

The objective of this study was to investigate how the crystal structure (monoclinic or hexagonal) and composition (oxidized or partially reduced) of WO_3 influenced photocatalytic behavior. Based on the obtained results, oxidized m–WO_3 (**m-WO_3 ox**) was the most active photocatalyst both in

the gas and liquid phase, while oxidized h–WO_3 (**h-WO_3 ox**) was the second in the activity. Reduced h–WO_3 (**h-WO_3 red**) and m–WO_3 (**m-WO_3 red**) had much lower activity.

The most decisive parameter on the photocatalytic properties of WO_3 was its composition, regardless of the crystallographic structure. Crystal structure (hexagonal or monoclinic) of WO_3 had only an indirect effect on photocatalysis, since different theoretical compositions belongs to the different structures. Oxidized m–WO_3 (in this case **m-WO_3 ox**) always has completely oxidized structure. In contrast, oxidized h–WO_3 is always in a slightly reduced state, as it contains trace amounts of NH_4^+ (or alkaline) ions, which are necessary to stabilize its structure. Therefore, oxidized m–WO_3 will always have a better photocatalytic performance than oxidized h–WO_3. Thus in contrast to TiO_2, where crystalline structure (rutile or anatase) is the key parameter on photocatalysis, in the case of WO_3 the composition of the samples is important. The crystal structure of WO_3 is important only to that extent, as it influences the composition of WO_3 samples.

As a consequence of our present and previous [35] investigations, we predict that (i) cubic WO_3 might also contain some stabilizing impurities in its channels along the structure. We propose this as cubic WO_3 is even more metastable [28] than h–WO_3, since it has not just one-, but three-dimensional channel-system along its structure. Thus, cubic WO_3 can also be a in a bit reduced state, like h–WO_3, and it can also have lower photocatalytic activity, than the fully oxidized m–WO_3. (ii) We also postulate that tungsten bronzes, in which W atoms are also reduced due to the presence of foreign cations [28,29,63], can have similarly lower photocatalytic activity, compared to oxidized m–WO_3. We note that it does not violate our theory that the $WO_{2.72}$ phase is also a good photocatalyst [64], though its W:O ratio is much lower than as in m–WO_3. $WO_{2.72}$ is a highly ordered, stoichiometric crystalline phase [65]. It does not have such defect sites, which are present in oxidized and reduced h–WO_3, and in reduced m–WO_3.

Supporting Information

Annealing study of $(NH_4)_xWO_{3-y}$; Figures of photocatalytic reactors; PL spectra of WO_3 samples with excitations at 230 and 270 nm. This material is available free of charge via the Internet at http://www.sciencedirect.com.

Acknowledgments

I. M. S. thanks for a Marie Curie Intra–European Fellowship (PIEF–GA–2009–235655) and a János Bolyai Research Fellowship of the Hungarian Academy of Sciences. TÉT_10-1-2011-0045; KPI–EU–GVOP–3.2.1.–2004–04–0224/3.0 KMA; GVOP–3.2.1.–2004–04–0210/3.0 and NHDP TÁMOP–4.2.1/B–09/1/KMR–2010–0002 grants are gratefully acknowledged.

References

[1] H. Tong, S. Ouyang, Y. Bi, N. Umezawa, M. Oshikiri, J. Ye, *Adv. Mater.* **24** (2012) 229-251.

[2] Q. Gu, J. Long, Y. Zhou, R. Yuan, H. Lin, X. Wang, *J. Catal.* **289** (2012) 88-99.

[3] Y.F. Li, Z.P. Liu, *J. Am. Chem. Soc.* **133** (2011) 15743.

[4] X. Chen, L. Liu, P.Y. Yu, S.S. Mao, *Science* **331** (2011) 746.

[5] G. Halasi, I. Ugrai, F. Solymosi, *J. Catal.* **281** (2011), 309-317.

[6] M. Grätzel, *Nature* **414** (2001) 338.

[7] D. Wang, Y. Liu, B. Yu, F. Zhou, W. Liu, *Chem. Mater.* **21** (2009) 1198.

[8] A. Fujishima, X. Zhang, D. Tryk, A. *Surf. Sci. Rep.* **63** (2008) 515.

[9] K. Rajeshwar, M.E. Osugi, W. Chanmanee, C.R. Chenthamarakshan, M.V.B. Zanoni, P. Kajitvichyanukul, R. Krishan–Ayer, *J. Photochem. Photobiol. C* **9** (2008) 171.

[10] A.L. Linsebigler, G. Lu, J.T. Yates Jr., *Chem. Rev.* **95** (1995) 735.

[11] K. Teramura, T. Tanaka, M. Kani, T. Hosokawa, T. Funabiki, *J. Mol. Catal. A* **28** (2004) 299.

[12] Z.G. Zhao, M. Miyauchi, *Angew. Chem. Int. Ed.* **47** (2008) 7051.

[13] T. Arai, M. Yanagida, Y. Konishi, A. Ikura, Y. Iwasaki, H. Sugihara, K. Sayama, *Appl. Catal. B* **84** (2008) 42.

[14] D.S. Bohle, C.J. Spina, *J. Am. Chem. Soc.* **131** (2009) 4397.

[15] K. Tang, J. Zhang, W. Yan, Z. Li, Y. Wang, W. Yang, Z. Xie, T. Sun, H. Fuchs, *J. Am. Chem. Soc.* **130** (2008) 2676.

[16] C.M. Foldvary, L. Wojnarovits, *Radiat. Phys. Chem.* **76** (2007) 1485.

[17] Y.P. Chen, S.Y. Liu, H.Q. Yu, H. Yin, Q.R. Li, *Chemosphere* **72** (2008) 532.

[18] M. Qamar, M.A. Gondal, Z.H. Yamani, *Catal. Commun.* **10** (2009) 1980.

[19] M.A. Rauf, S.S. Ashraf, *J. Hazard. Mater.* **166** (2009) 6.

[20] A.N.M. Bagyo, W. Andayani, H. Winarno, E. Katrin, Y.S. Soebianto, *Int. J. Env. Consc. Design Manufac.* **12** (2004) 45.

[21] S.J. Hong, H. Jun, P.H. Borse, J.S. Lee, *Int. J. Hydrogen Energ.* **34** (2009) 3234.

[22] V. Loddo, G. Marcì, C. Martín, L. Palmisano, V. Rives, A. Sclafani, *Appl. Catal. B* **20** (1999) 29.

[23] S. Bakardjieva, J. Šubrt, V. Štengl, M.J. Dianez, M.J. Sayagues, *Appl. Catal. B* **58** (2005) 193.

[24] N. Kislov, J. Lahiri, H. Verma, D.Y. Goswami, E. Stefanakos, M. Batzill, *Langumir* **25** (2009) 3310.

[25] F. Chen, Y. Xie, J. Hel, J. Zhao, *J. Photochem. Photobi. A* **138** (2001) 139.

[26] O. Akhavan, R. Azimirad, *Appl. Catal. A* **369** (2009) 77.

[27] J. Herrmann, *Catal. Today* **53** (1999) 115.

[28] E. Lassner, W.D. Schubert, *Tungsten. Properties, Chemistry, Technology of the Element, Alloys, and Chemical Compounds* Kluwer Academic/Plenum Publishers: New York, 1999.

[29] R.J D. Tilley, *Int. J. Refract. Met. Hard. Mater.* **13** (1995) 93.

[30] G. Xin, W. Guo, T. Ma, *Appl. Surf. Sci.* **256** (2009) 165.

[31] M. Qamar, M.A. Gondal, Z.H. Yamani, *Catal. Commun.* **11** (2010) 768.

[32] J. Yu, L. Qi, B. Cheng, X. Zhao, *J. Hazard. Mater.* **160** (2008) 621.

[33] H. Wang, P. Xu, T. Wang, *Mater. Design* **23** (2002) 331.

[34] I.M. Szilágyi, S. Saukko, J. Mizsei, A.L. Tóth, J. Madarász, G. Pokol, *Solid State Sci.* **12** (2010) *1857*.

[35] I.M. Szilágyi, J. Madarász, G. Pokol, S. Saukko, J. Mizsei, P. Király, G. Tárkányi, A.L. Tóth, A. Szabó, K. Varga–Josepovits, *Chem. Mater.* **20** (2008) 4116.

[36] Y. Li, X. Su, J. Jian, J. Wang, *Ceram. Int.* **36** (2010) 1917.

[37] C. Balázsi, K. Sedlácková, E. Llobet, R. Ionescu, *Sens. Actuat. B* **133** (2008) 151.

[38] I.M. Szilágyi, F. Hange, J. Madarász, G. Pokol, *Eur. J. Inorg. Chem.* 17 (2006) 3413.

[39] D.G. Cory, W.M. Ritchey, *J. Magn. Reson.* **80** (1988) 128.

[40] I.M. Szilágyi, J. Pfeifer, C. Balázsi, A.L. Tóth, K. Varga–Josepovits, J. Madarász, G. Pokol, *J. Therm. Anal. Calorim.* 94 (2008) 499.

[41] M.F. Daniel, B. Desbat, J.C. Lassegues, B. Gerand, M. Figlarz, *J. Solid State Chem.* **67** (1987) 235.

[42] C. Santato, M. Odziemkowski, M. Ulmann, J. Augustynski, *J. Am. Chem. Soc.* **123** (2001) 10639.

[43] C.V. Ramana, S. Utsunomiya, R.C. Ewing, C.M. Julien, U. Becker, *J. Phys Chem. B* **110** (2006) 10430.

[44] T. Siciliano, A. Tepore, G. Micocci, A. Serra, D. Manno, E. Filippo, *Sens. Actuat. B* **133** (2008) 321.

[45] M.J. Pelletier, *Appl. Spectrosc.* **57** (2003) 20A.

[46] P. Shen, N. Chi, K.Y. Chan, *J. Mater. Chem.* **10** (2000) 697.

[47] I.M. Szilágyi, L. Wang, P.I. Gouma, C. Balázsi, J. Madarász, G. Pokol, *Mater. Res. Bull.* **44** (2009) 505.

[48] I.M. Szilágyi, J. Madarász, G. Pokol, F. Hange, G. Szalontai, K. Varga–Josepovits, A.L. Tóth, *J. Therm. Anal. Calorim.* **97** (2009) 11.

[49] I.M. Szilágyi, I. Sajó, P. Király, G. Tárkányi, A.L. Tóth, A. Szabó, K. Varga–Josepovits, J. Madarász, G. Pokol, *J. Therm. Anal. Calorim.* **98** (2009) 707.

[50] H.J. Lunk, B. Ziemer, M. Salmen, D. Heidemann, *Int. J. Refract. Met. Hard Mater.* **12** (1993–1994) 17.

[51] H.J. Lunk, M. Salmen, D. Heidemann, *Int. J. Refract. Met. Hard Mater.* **16** (1998) 23.

[52] L. Palmisano, V. Augugliaro, A. Sclafani, M. Schiavello, *J. Phys. Chem.* **92** (1988) 6710.

[53] J.A. Navio, J.J. Testa, P. Djedjeian, J.R. Padron, D. Rodriguez, M.I. Litter, *Appl. Catal. A* **178** (1999) 191.

[54] J.M. Hermann, J. Disdier, P. Pichat, *Chem. Phys. Lett.* **108** (1984) 618.

[55] O. Carp, C.L. Huisman, A. Reller, *Prog. Solid State Chem.* **32** (2004) 33.

[56] W. Hu, Y. Zhao, Z. Liu, C.W. Dunnill, D.H. Gregory, Y. Zhu, *Chem. Mater.* **20** (2008) 5657.

[57] J. Wang, P.S. Lee, J. Ma, *J. Cryst. Growth* **311** (2009) 316.

[58] J.H. Ha, P. Muralidharan, D.K. Kim, *J. Alloy. Comp.* **475** (2009) 446.

[59] S.H. Lee, H.M. Cheong, C.E. Tracy, A. Mascarenhas, D.K. Benson, S.K. Deb *Electrochim. Acta* **44** (1999) 3111.

[60] E.A. Kozlova, P.G. Smirniotis, A.V. Vorontsov, *J. Photochem. Photobio. A* **162** (2004) 503.

[61] K. Goss, S. Eisenreich, *J. Environ. Sci. Technol.* **30** (1996) 2135.

[62] R. Azimirad, N. Naseri, O. Akhavan, A.Z. Moshfegh, *J. Phys. D* **40** (2007) 1134.

[63] P.G. Dickens, M.S. Whittingham *Quart. Rev.* **22** (1968) 30.

[64] F. Kojin, M. Mori, Y. Noda, M. Inagaki, *Appl. Catal. B* **78** (2008) 202.

[65] I.M. Szilágyi, J. Madarász, F. Hange, G. Pokol, *J. Therm. Anal. Calorim.* **88** (2007) 139.

Captions

Table 1. Preparation conditions from $(NH_4)_xWO_{3-y}$, specific surfaces, particle sizes and W oxidation states of WO_3 samples

Figure 1. (a) Structure of h– and m–WO_3; (b) Photoimages of WO_3 samples showing their yellow or dark blue color; c) XRD patterns of WO_3 samples; (d) Raman spectra of WO_3 samples

Figure 2. SEM images of WO_3 samples

Figure 3. TEM images, ED patterns and HRTEM images of WO_3 samples. Indices of ED patterns are according to h–WO_3 (**h-WO_3 ox**, **h-WO_3 red**) and m–WO_3 (**m-WO_3 ox**, **m-WO_3 red**). HRTEM images reveal (100) and (020) fringes for h–WO_3 and m–WO_3, respectively.

Figure 4. (a) ^{1}H–MAS NMR spectra of WO_3 samples and the precursor $(NH_4)_xWO_{3-y}$; (b) Deconvolution of the ^{1}H–MAS NMR spectrum of **h-WO_3 ox**

Figure 5. (a) Diffuse reflectance UV–VIS and (b) PL spectra (using excitation at 340 nm) of WO_3 samples

Figure 6. Gas phase photocatalysis results of WO_3 samples showing the amount of CO_2 produced photocatalytically from acetone at various relative humidity (RH) levels

Figure 7. Relative absorbance curves of methyl orange (MO) decomposed photocatalytically by the WO_3 samples (measured by UV–VIS at 465 nm)

Table

Table 1. Preparation conditions from $(NH_4)_xWO_{3-y}$, specific surfaces, particle sizes, W oxidation states and ratio of surface $O^{2-}/OH^-/H_2O$ species of WO_3 samples

Name	Crystalline phase	Oxidation state, color	Atmosphere	T (°C)	m^2/g	Particle size [a], nm	Particle size [b], nm	$W^{6+}/W^{5+}/W^{4+}$ atom% [c]	W [d]	Surface $O^{2-}/OH^-/H_2O$, % [e]
h-WO_3 ox	hexagonal WO_3	oxidized, yellow	Air	470	11	76	50–70	97.3/1.7/1.1	5.96	1.00/0.52/0.18
h-WO_3 red	hexagonal WO_3	reduced, blue	N_2	550	13	65	50–70	93.1/4.6/2.3	5.91	1.00/0.33/0.12
m-WO_3 ox	monoclinic WO_3	oxidized, yellow	Air	600	6.5	129	60–90	100.0/0.0/0.0	6.00	1.00/0.70/0.23
m-WO_3 red	monoclinic WO_3	reduced, blue	N_2	650	12	70	50–70	84.5/11.1/4.3	5.80	1.00/0.31/0.10

[a] Mean particle size determined by N_2-BET, [b] Mean particle size determined by TEM and SEM; [c] Oxidation sates of W were determined by XPS from $W4f_{7/2}$ peaks (37.2, 36.1, 34.9 eV for W^{6+}, W^{5+}, W^{4+}, respectively), and from $W4f_{5/2}$ peaks (35.1, 33.7, 32.8 eV for W^{6+}, W^{5+}, W^{4+}, respectively); [d] Average oxidation number; [e] The amounts of surface $O^{2-}/OH^-/H_2O$ species were determined by XPS from O1s peak (530.9, 531.6, 532.5 eV for O^{2-}, OH^-, H_2O, respectively)

Figure 1

Click here to download high resolution image

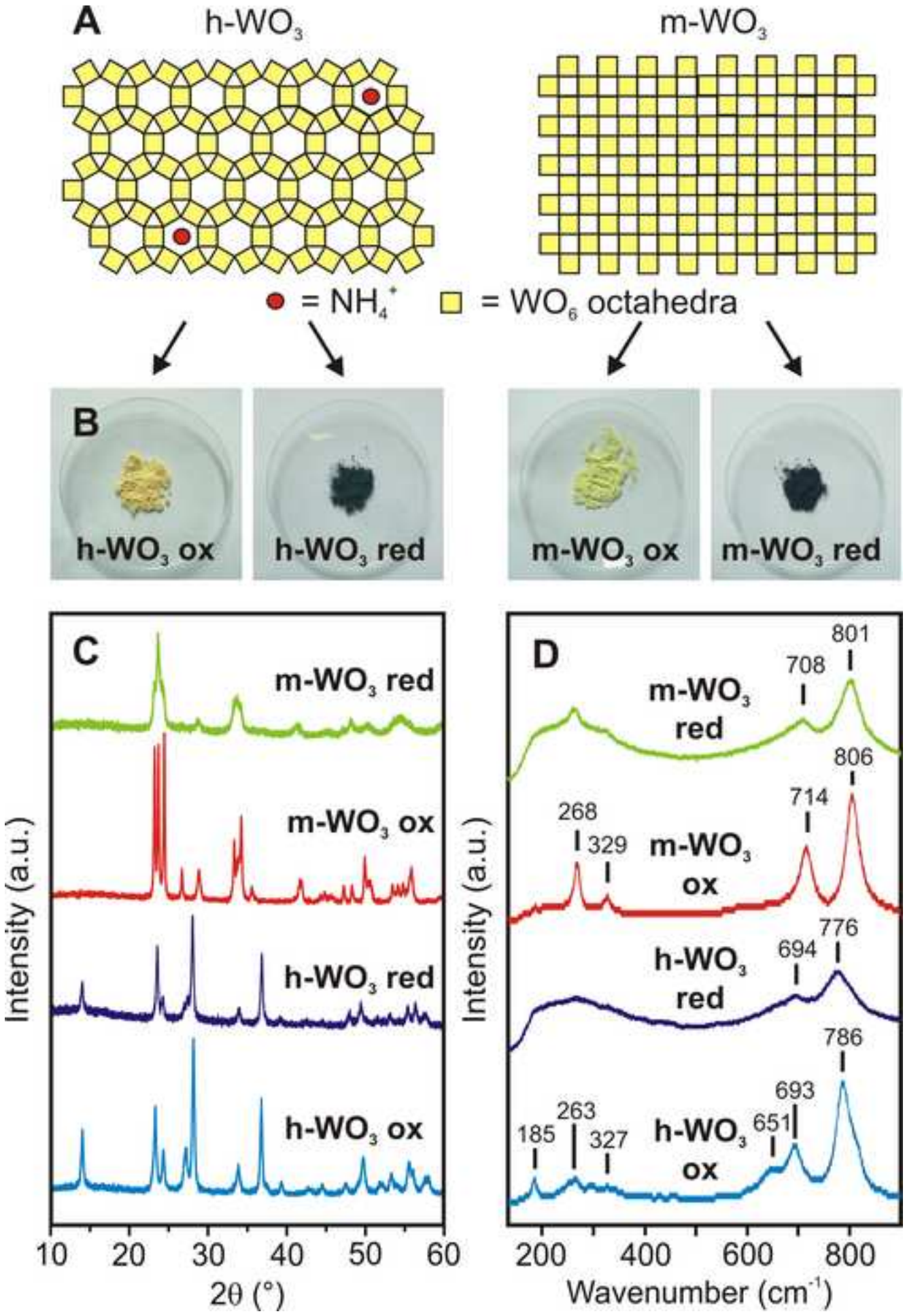

Figure 2

Click here to download high resolution image

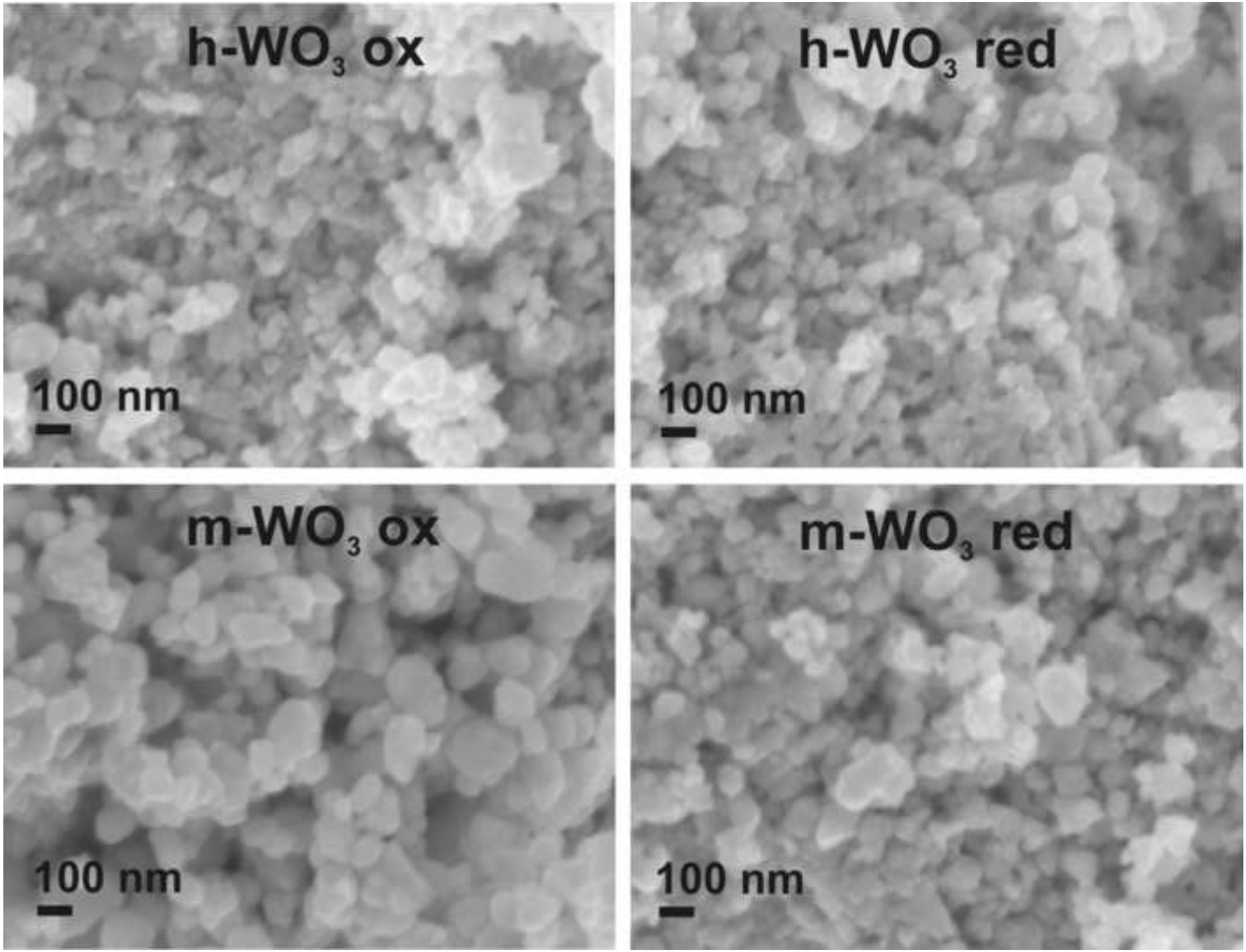

Figure 3

Click here to download high resolution image

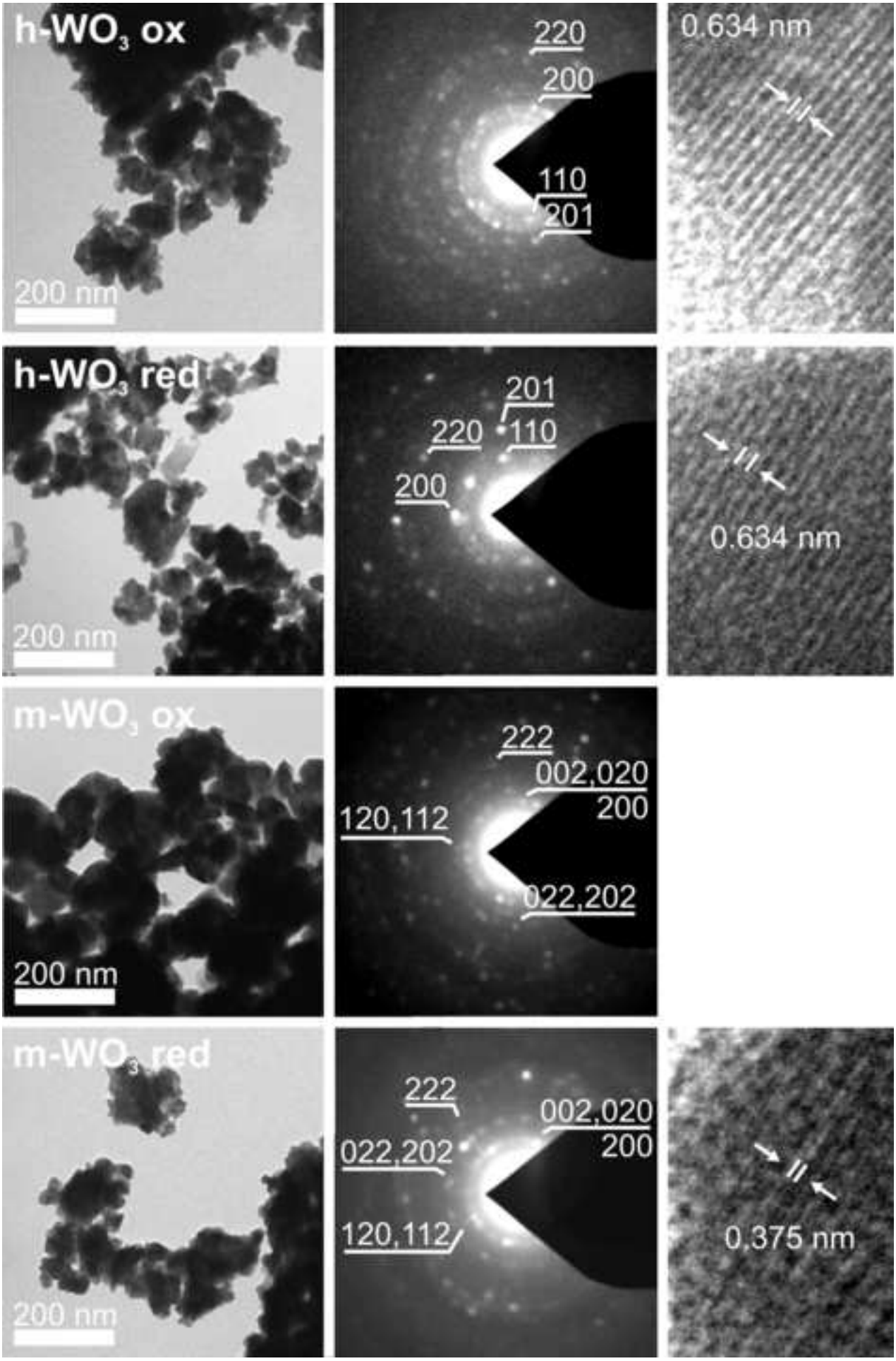

Figure 4

Click here to download high resolution image

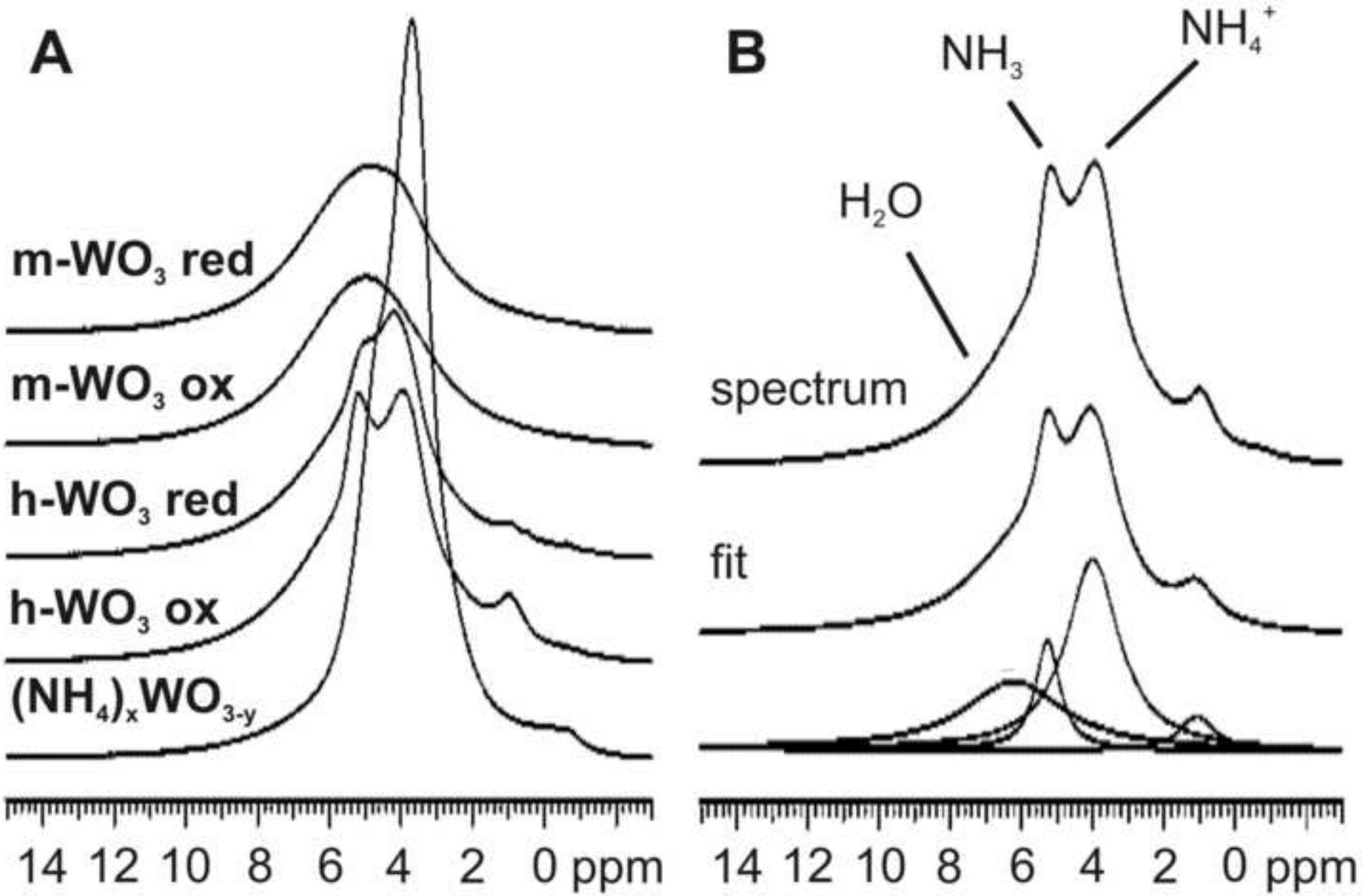

Figure 5

Click here to download high resolution image

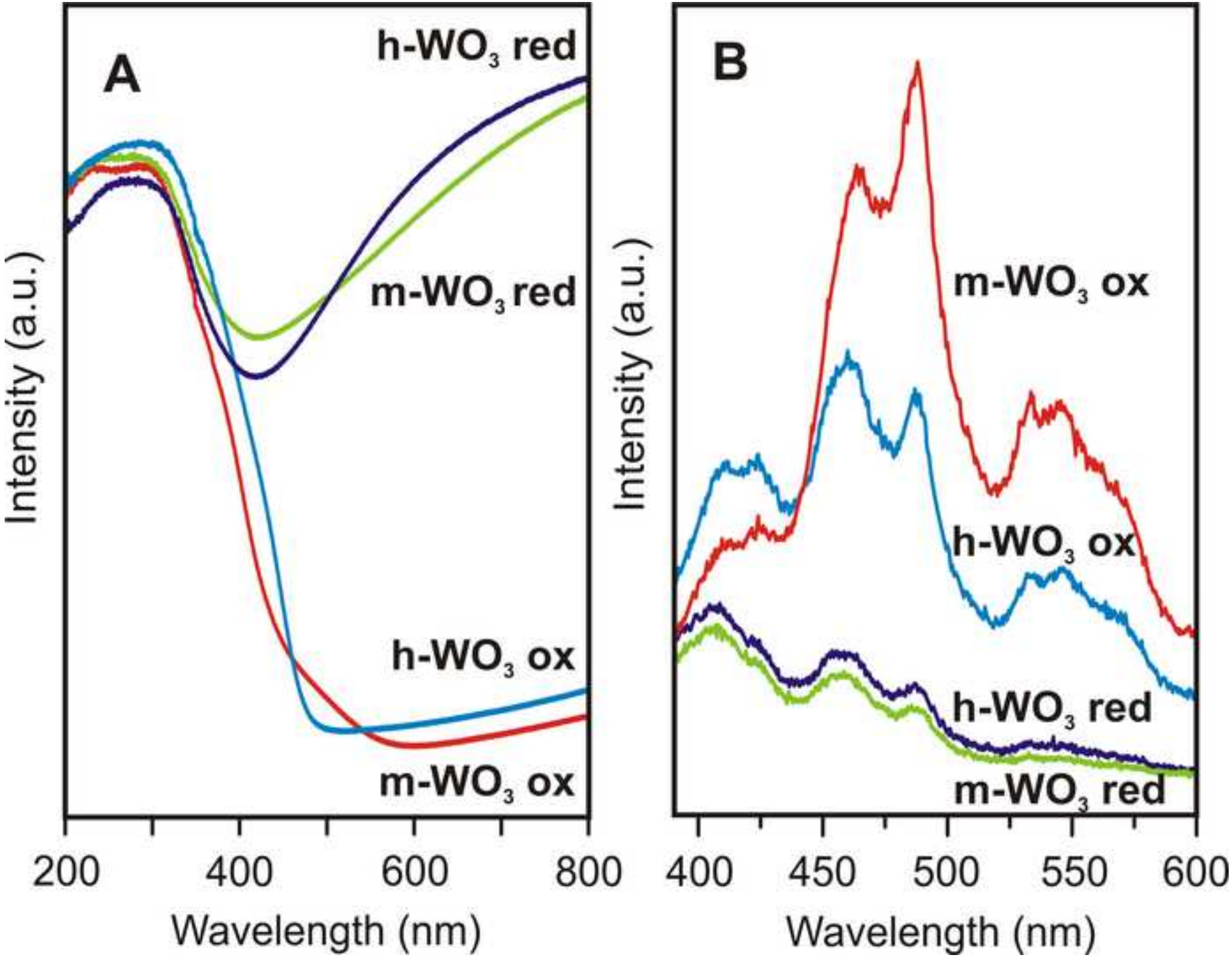

Figure 6

Click here to download high resolution image

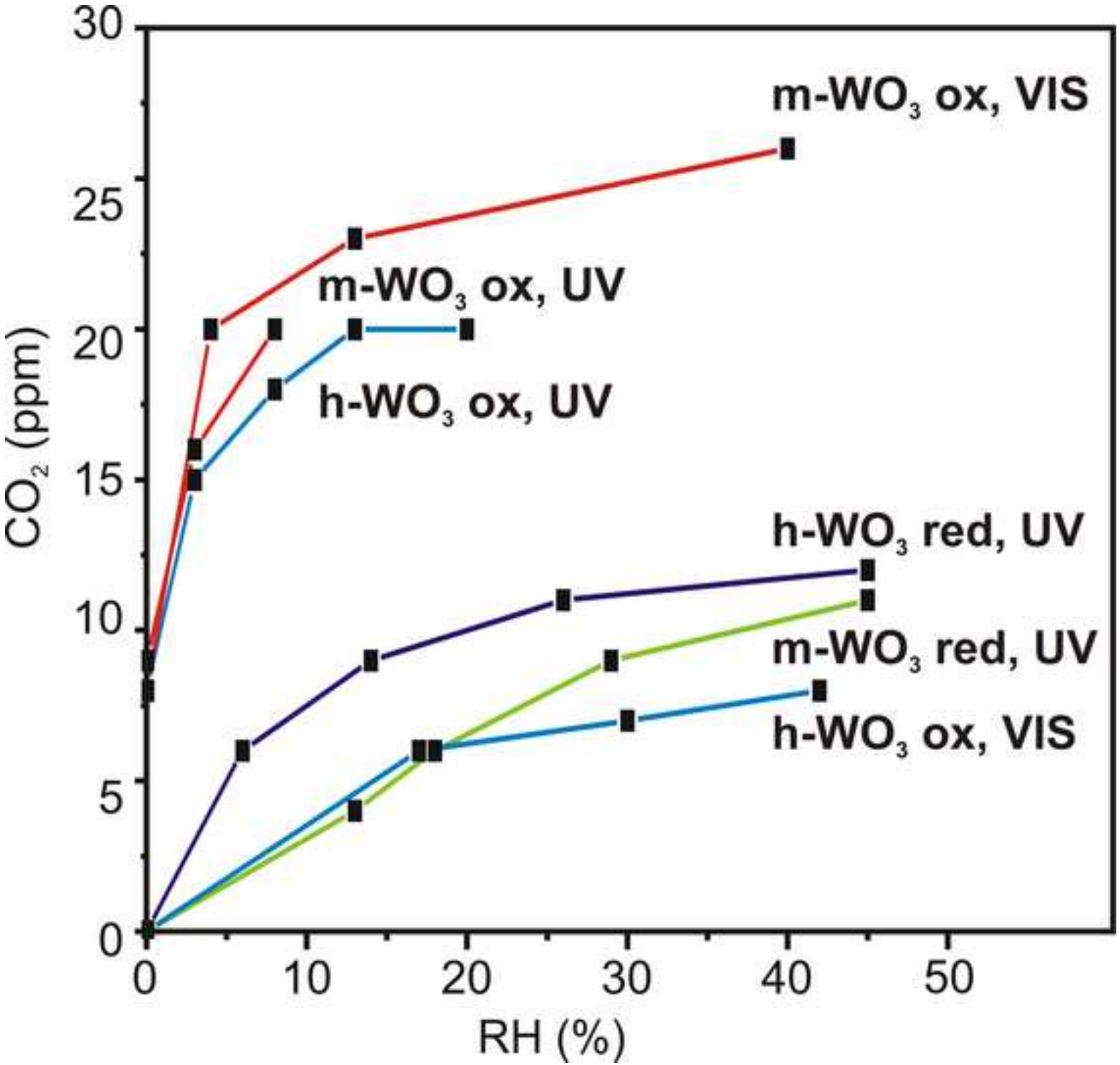

Figure 7

Click here to download high resolution image

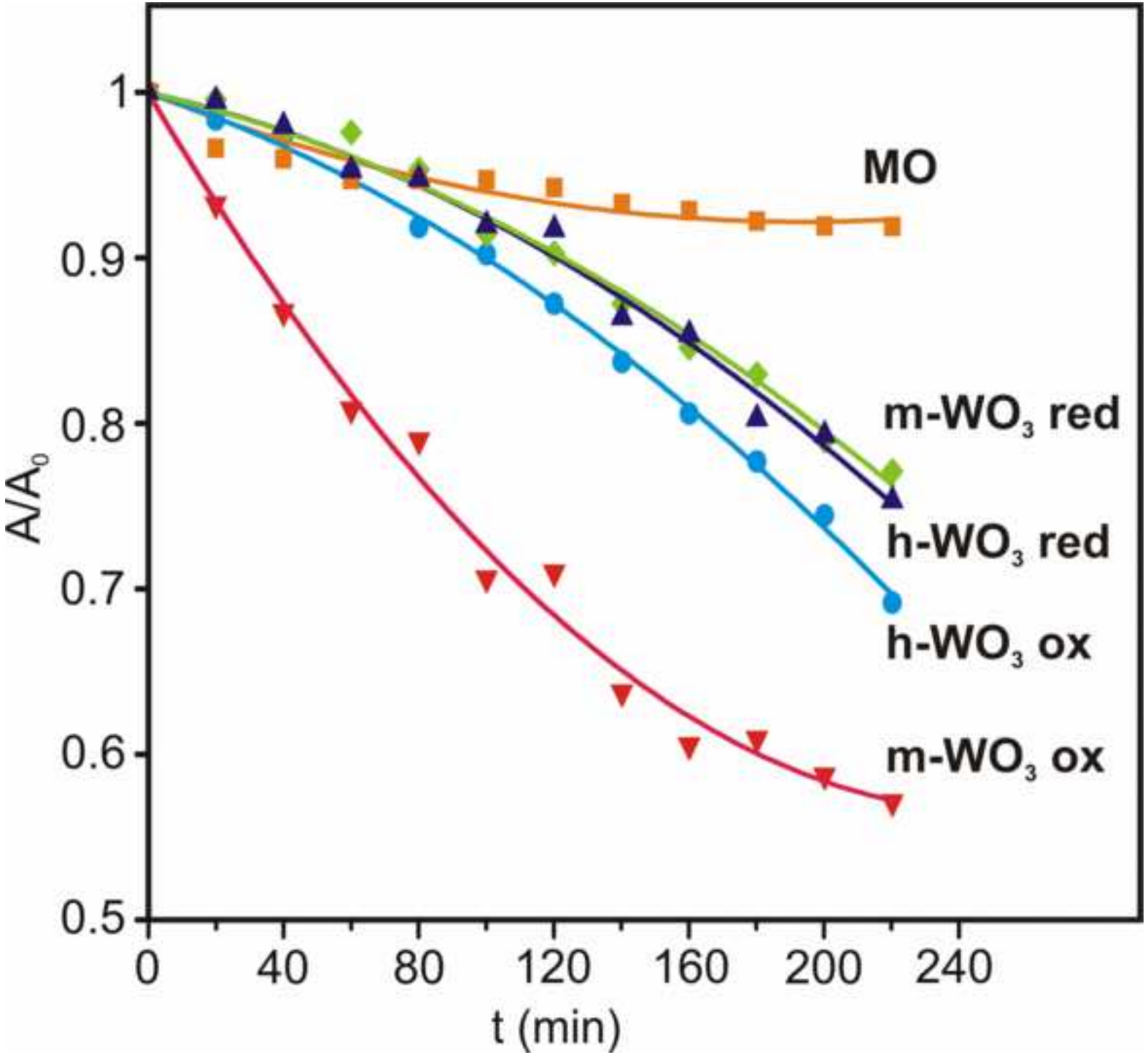

Supplementary Material

Click here to download Supplementary Material: Revised Supporting information WO3 photocatalysis J Catal.pdf